nature photonics

LETTERS

PUBLISHED ONLINE: 21 MARCH 2016 | DOI: 10.1038/NPHOTON.2016.44

Real-space mapping of tailored sheet and edge plasmons in graphene nanoresonators

A. Y. Nikitin[1,2]*, P. Alonso-González[1,3], S. Vélez[1], S. Mastel[1], A. Centeno[4], A. Pesquera[4], A. Zurutuza[4], F. Casanova[1,2], L. E. Hueso[1,2], F. H. L. Koppens[5,6] and R. Hillenbrand[2,7]*

Plasmons in graphene nanoresonators have many potential applications in photonics and optoelectronics, including room-temperature infrared and terahertz photodetectors, sensors, reflect arrays or modulators[1–7]. The development of efficient devices will critically depend on precise knowledge and control of the plasmonic modes. Here, we use near-field microscopy[8–11] between λ_0 = 10–12 μm to excite and image plasmons in tailored disk and rectangular graphene nanoresonators, and observe a rich variety of coexisting Fabry–Perot modes. Disentangling them by a theoretical analysis allows the identification of sheet and edge plasmons, the latter exhibiting mode volumes as small as $10^{-8}\lambda_0^3$. By measuring the dispersion of the edge plasmons we corroborate their superior confinement compared with sheet plasmons, which among others could be applied for efficient 1D coupling of quantum emitters[12]. Our understanding of graphene plasmon images is a key to unprecedented in-depth analysis and verification of plasmonic functionalities in future flatland technologies.

At infrared and terahertz frequencies doped graphene can support electrically tunable graphene plasmons (GPs)—electromagnetic fields coupled to charge carrier oscillations—with extremely short wavelengths and large confinement[13–17]. For that reason, graphene shows great potential for controlling radiation on the nanometre scale[18], which benefits the development of highly sensitive spectroscopy[3] and detection[19–21] applications. The electromagnetic field concentration achieved by GPs can be further enhanced by fabricating nanostructures that act as Fabry–Perot resonators for GPs (for example disks or ribbons)[1,2,6,7,22], favouring strong absorption in arrays of the resonators (up to 40%)[7]. Until now localized plasmonic modes in graphene ribbons and disks have mainly been analysed experimentally by far-field spectroscopy[1,2,6,7,22], however, neither the mode structure nor the unique plasmonic edge modes are accessible with this technique. A comprehensive experimental characterization of graphene plasmonic nanoresonators and their sheet and edge modes has thus been not achieved yet. On the other hand, plasmonic edge modes have been shown to propagate along the sharp edges of gold films, graphene and two-dimensional (2D) electron gases[11,23–28] and to provide stronger confinement of the electromagnetic fields compared with sheet plasmons.

Here we image and analyse the near-field structure of both plasmonic sheet and edge modes in graphene disks and rectangular nanoresonators. We employ scattering-type scanning near-field optical microscopy (s-SNOM), which is currently the only available tool for real-space imaging of the propagation and confinement characteristics of GPs[8–11,29]. The lack of a detailed understanding of graphene plasmonic s-SNOM contrasts, however, has so far prevented a comprehensive analysis of plasmon modes in graphene nanostructures. We tackled this problem with 3D numerical simulations, revealing that puzzling negative plasmonic s-SNOM contrasts[8–10] are governed by a spatially varying Fano-like interference between the near field of the probing tip and the GPs. This finding enables us to disentangle the rich variety of coexisting Fabry–Perot modes, allowing the edge and sheet modes to be identified, as well as separated either spatially or spectrally.

Figure 1a illustrates s-SNOM imaging of localized GPs. A metal tip is used as a near-field probe. It concentrates the incident field to a nanoscale spot at the tip apex, providing the necessary momentum to excite GPs in a graphene nanoresonator. Interaction of the resonating GP field with the tip modifies the tip scattered field. Recording the magnitude of this field as a function of the tip position thus yields real-space near-field images $|E_s(x,y)|$ (see Methods).

For identifying plasmon modes and resonances, we imaged a set of disks with a diameter d increasing from 50 to 450 nm, tailored to exhibit GP resonances at the two illumination wavelengths $\lambda_{0,1}$ = 11.06 μm and $\lambda_{0,2}$ = 11.31 μm (Fig. 1c). For both wavelengths we observe several significant near-field features: a bright ring and a dark centre for the small disks (50 to 75 nm), a dark ring and a bright centre for medium sized disks (150 to 200 nm) and a dark centre for disks with a diameter around 350 nm. To better understand the experimental near-field images, we plot the near-field signal $|E_s|$ at two fixed tip positions (the centre and edge of the disks) as a function of d (Fig. 1g,h). In the disk centre, we find strong peaks around d = 200 nm, providing clear evidence of a GP resonance (Fig. 1g). A resonance behaviour is also found at the edge (Fig. 1h), but the peaks emerge at much smaller disk diameters (around d = 75 nm), indicating that a different plasmonic mode is excited. The peaks shift to larger disk sizes when the illumination wavelength is increased from $\lambda_{0,1}$ to $\lambda_{0,2}$, which is a typical characteristic for plasmon excitations[1,7]. These results show that the near-field images of the disks comprise the position-dependent excitation of different plasmonic modes, which challenges the interpretation of the observed GP patterns.

We analyse the near-field images with the help of numerical electromagnetic calculations (for details see Methods and Supplementary Section A). We approximate the illuminated tip with a dipole source above the graphene disk located on a substrate (Fig. 1b). By plotting the near field (NF) below the dipole as a function of its position, we obtain simulated near-field images, $|E_z(x,y)|$ (Fig. 1d), that are in excellent agreement with $|E_s(x,y)|$ (Fig. 1c). A good agreement is also found between the experimental and calculated resonance peaks when the tip and the dipole, respectively, are located in the disk centre (Fig. 1g,i). When the dipole is located at the disk edges,

[1]CIC nanoGUNE, 20018 Donostia-San Sebastián, Spain. [2]IKERBASQUE, Basque Foundation for Science, 48011 Bilbao, Spain. [3]Institute of Physics, Chinese Academy of Science, Beijing 100190, China. [4]Graphenea SA, 20018 Donostia-San Sebastián, Spain. [5]ICFO-Institut de Ciències Fotòniques, The Barcelona Institute of Science and Technology, 08860 Castelldefels, Barcelona, Spain. [6]ICREA – Institució Catalana de Recerça i Estudis Avancats, E-08010 Barcelona, Spain. [7]CIC NanoGUNE and UPV/EHU, 20018 Donostia-San Sebastian, Spain. *e-mail: a.nikitin@nanogune.eu; r.hillenbrand@nanogune.eu

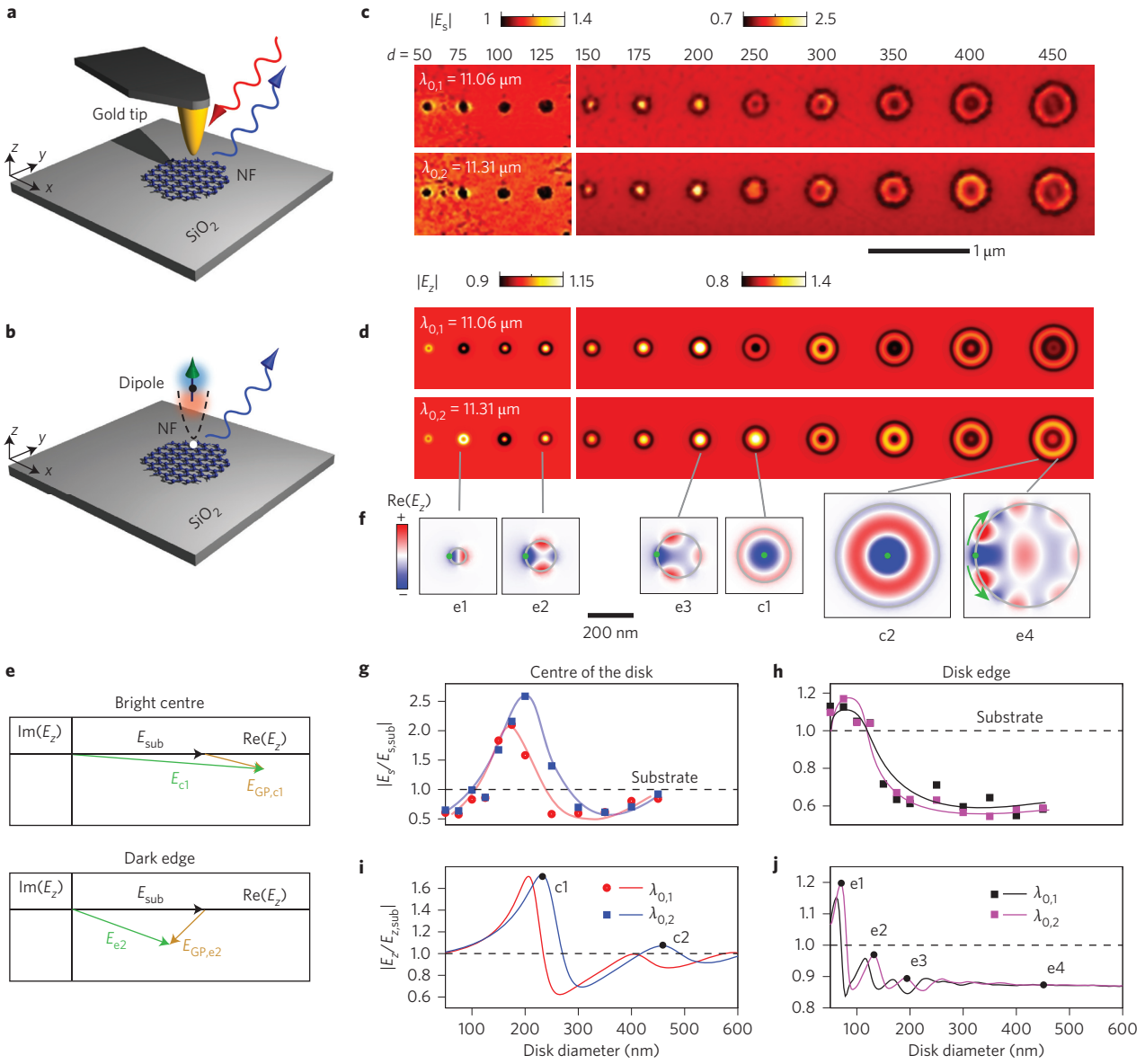

Figure 1 | GP modes in graphene disk nanoresonators on an SiO_2 substrate. a,b, Schematics of the experiment (**a**) and simulation model (**b**). **c,d**, Experimental (**c**) and simulated (**d**) near-field images at the wavelengths $\lambda_{0,1} = 11.06$ μm and $\lambda_{0,2} = 11.31$ μm. **e**, Schematics illustrating the constructive and destructive interference of the dipole's near field (E_{sub}) and the GP field (E_{GP}), respectively, yielding the peak c1 in **i**, and peak e2 in **j**. **f**, Near-field distributions 15 nm above the graphene disks induced by the dipole located at either the centre (denoted by c1, c2) or the edge (denoted by e1, e2, e3 and e4). The dipole locations are marked by green dots. They correspond to the modes c1, c2 and e1–e4 marked by black dots in **i** and **j**. **g–j**, Measured and calculated near-field magnitude in the disk centre and at the edge for $\lambda_{0,1}$ and $\lambda_{0,2}$. Simulations assume $E_F = 0.33$ eV and $\tau = 0.1$ ps.

the model yields a strong peak (e1) for small diameters (Fig. 1j), which is also clearly seen in the experiment (Fig. 1h). The higher-order resonances seen in the simulations (e2, e3 in Fig. 1j) do not appear in the experiment (Fig. 1h), which we attribute to the limited number of data points and signal-to-noise ratio. Having established its validity, we can apply the model to reliably connect the near-field image contrasts with the various GP modes.

To recognize the individual GP modes, we calculated the spatial near-field distribution above selected graphene disks for different fixed dipole positions (Fig. 1f). When the dipole (position marked by a green dot) is located at the centre of one of the brightest disks ($d = 250$ nm), we clearly recognize a circularly symmetric breathing mode (c1 in Fig. 1f) that can be assigned to the strong resonance peak in Fig. 1g,i. In contrast, a completely different plasmon mode appears when the dipole is located at the edge of the same disk (e3, Fig. 1f): the field oscillations are strongly confined to the edge and propagate along it, obviously revealing an edge mode. Perpendicular to the edge, the fields decay by a factor of $1/e$ at a distance of $\lambda_e/2\pi = 30$ nm $= \lambda_0/370$, where $\lambda_e = 190$ nm is the wavelength of the edge plasmons. With decreasing diameter, the number of the field oscillations decreases (e1, e2). Around $d = 100$ nm, the edge mode transforms into the fundamental dipolar mode (e1), resulting in the resonance peak at $d = 75$ nm (Fig. 1h,j) and a bright ring decorating the graphene edge that can be seen in both experiment and simulation (Fig. 1c,d). These results provide direct evidence that the tip can efficiently excite and probe both plasmonic sheet and edge modes in graphene nanoresonators.

Surprisingly, we find in both experiment and theory that the disk edge appears darker than the substrate for all diameters $d > 100$ (referred to as negative near-field contrast), although edge plasmons are excited (see e4 in Fig. 1f for an example). Similarly, the excitation of the breathing mode (c1, Fig. 1f) yields negative contrasts for disk

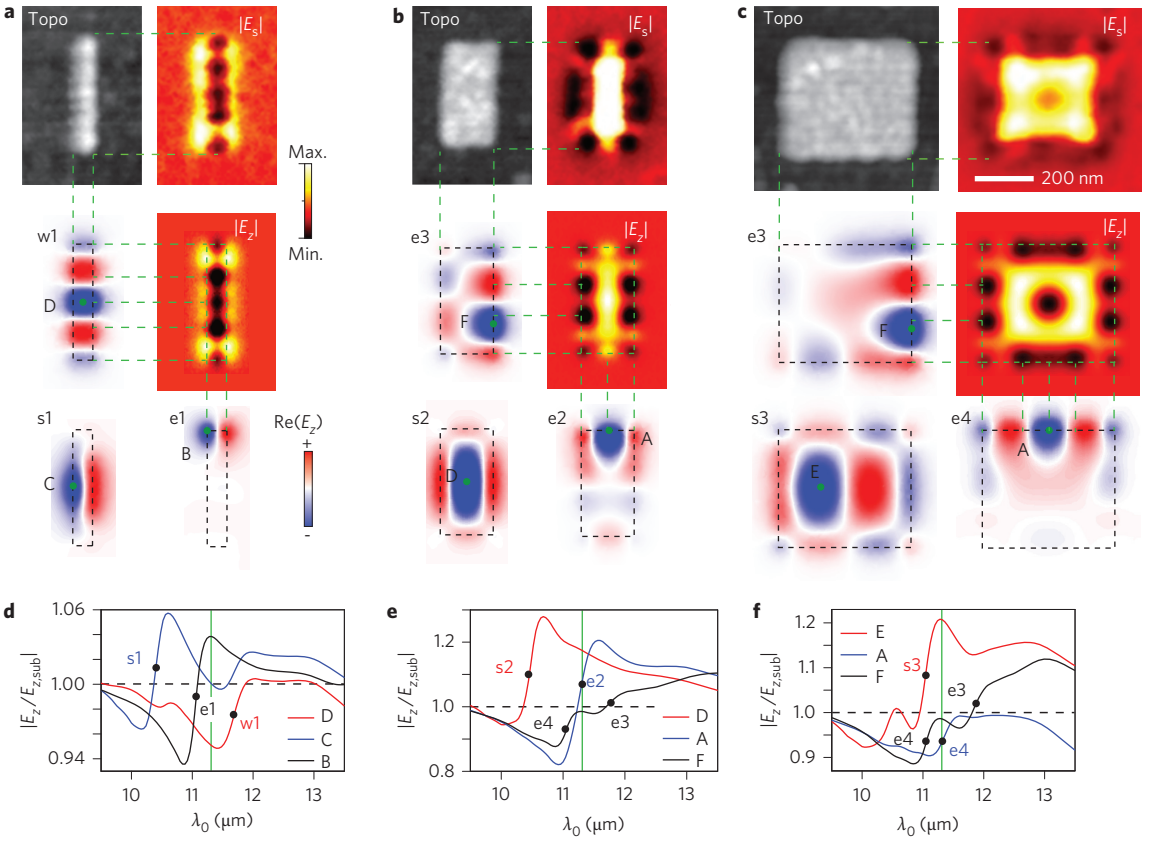

Figure 2 | GP modes in rectangular graphene nanoresonators on a 5-nm-thick SiO_2 film on a CaF_2 substrate. a–c, Topography (top left), experimental near-field image ($|E_s|$, top right), calculated near-field image ($|E_z|$, middle right) and calculated near-field distributions when the dipole is placed at positions marked by green dot for different resonator sizes: 394 × 73 nm (**a**), 360 × 180 nm (**b**) and 400 × 450 nm (**c**). λ_0 = 11.31 μm (marked by the vertical green line in **d–f**). w1 marks the fundamental waveguiding mode, s1–s3 mark the first-order to third-order transversal sheet mode and e1–e4 mark the first-order to fourth-order edge modes. **d–f**, Corresponding near-field spectra calculated at the points A–F (marked by green dots in the near-field distributions) for the resonators shown in **a–c**. To provide the closest match between the experimental and simulated near-field images we used Fermi energies of E_F = 0.30 eV (**a**,**d**), E_F = 0.28 eV (**b**,**e**) and E_F = 0.31 eV (**c**,**f**). Relaxation time τ = 0.1 ps.

diameters larger than 300 nm (that is, the disk centre is darker than the substrate). Considering that the tip-induced GP excitation in the nanoresonators is a resonant process, we can assume that $E_{z,GP}$ is phase-shifted compared with the dipole's near field above the substrate, $E_{z,sub}$. This phase shift depends on the disk size relative to the resonant disk size, and can lead to constructive or destructive interference, yielding positive or negative near-field contrast, respectively. To corroborate the phase shift and interference effects, we calculated both $E_{z,sub}$ and $E_{z,GP}$ (see Supplementary Section A). The results obtained for both e2 and c1 modes are illustrated (for clarity, not quantitatively) in the complex plane (Fig. 1e). We find that small phase shifts between $E_{z,sub}$ and $E_{z,GP}$ (breathing mode c1, upper panel of Fig. 1e) increase the amplitude (length of the arrows) of the total near field above graphene, $E_z = E_{z,sub} + E_{z,GP}$. Conversely, for strong phase shifts (edge mode e2, lower panel of Fig. 1e) the total near-field amplitude is reduced, which shows that interference of $E_{z,sub}$ and $E_{z,GP}$ can make plasmon patterns appear in negative contrast in the near-field images. This effect can be interpreted as a Fano-like resonance[30], where a non-resonant scattering process ($E_{z,sub}$) interferes with a resonant scattering process ($E_{z,GP}$). The Fano-like resonance can be appreciated by the asymmetric line shapes in Fig. 1g,i. On the basis of this new understanding of the GP near-field contrasts, we are able to properly recognize the specific GPs modes comprising the near-field images. More specifically, our analysis explains that the edges of large graphene flakes can appear dark in near-field images (as experimentally observed in Fig. 1c and in refs 8–10) owing to the excitation of edge modes and their destructive interference with the dipole's near field (Supplementary Fig. 1b in Supplementary Section A).

We further studied GP modes in graphene rectangles, constituting another canonical and important plasmonic resonator structure[31]. The experimental near-field images, $|E_s|$, for three rectangles of different widths w but approximately equal lengths (400 nm) are shown in Fig. 2a–c (top right), all recorded at λ_0 = 11.31 μm. We observe a rich variety of bright and dark features, including black dots decorating the edges, that are well reproduced by simulations (Fig. 2a–c, middle right, $|E_z|$) based on the model described above. We analyse the near-field images by calculating the near field below the dipole as a function of λ_0 for different dipole positions (marked by green dots and labeled A–F in Fig. 2). In the resulting spectra (Fig. 2d–f) we find several peaks close to the imaging wavelength (λ_0, marked by vertical lines in Fig. 2d–f), indicating the resonant excitation of different GP modes. Because of their spectral overlap, the monochromatic near-field images exhibit complex GP interference patterns. As before in Fig. 1, the asymmetric line shape of the peaks can be explained by the Fano-like interference between the tip-induced GPs, $E_{z,GP}$, and the field below the dipole, $E_{z,sub}$ (see discussion above).

For identifying the GP modes and recognizing them within the near-field images, we calculated the spatial near-field distributions above the resonators that are generated by the dipole located at positions A–F. To isolate the modes, the calculations were performed at the individual peak wavelengths. The near-field distributions (labelled w1, s1–s3 and e1–e4 in Fig. 2) clearly reveal the typical pattern of fundamental and higher-order resonator modes. Similar

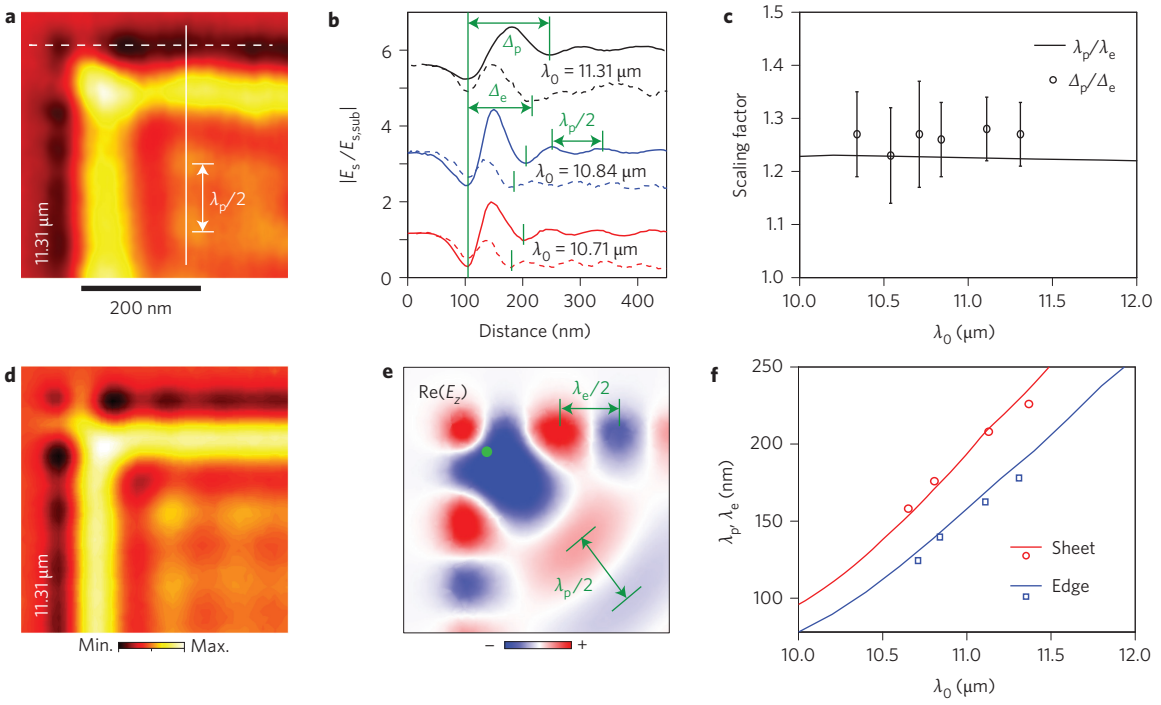

Figure 3 | Dispersion of sheet and edge GPs in a large graphene structure on an SiO_2 substrate. a, Experimental near-field image at $\lambda_0 = 11.31$ μm. **b**, The dashed curves represent the individual line profiles along the horizontal white line in **a**, and solid curves represent averages of 20 individual line profiles in proximity to the solid white line in **a**. **c**, Averaged ratio Δ_p/Δ_e obtained from individual near-field profiles such as the ones shown in **b**. The error bars show the standard deviation, and the line shows the calculated ratio λ_p/λ_e. **d**, Calculated near-field image. **e**, The near-field distribution generated by a dipole placed above the graphene rectangle at the position marked by the green dot. **f**, Dispersion (lines for the theory and symbols for the experiment) of the sheet and edge GPs. Simulations assume $E_F = 0.33$ eV and $\tau = 0.1$ ps. Experimental data for $\lambda_0 < 10.6$ μm are missing, because λ_p could not be measured.

to the disk resonators, we find direct evidence for sheet modes (s1–s3), edge modes (e1–e4) and the fundamental waveguiding mode w1 (the numbers indicate the order of the mode).

In the near-field images $|E_z|$ of the large resonators (Fig. 2b,c) we recognize the edge modes as rows of black dots decorating the edges. Indeed, comparison with the edge mode patterns (near-field distributions e3 and e4 in Fig. 2a) shows that the near-field maxima and minima in e3 and e4 agree well with the black dots in $|E_z|$ (see dashed green lines). We explain the appearance of the black dots (near-field signal oscillations revealing a standing wave pattern) by Fabry–Perot resonances of edge modes being launched by the tip and reflected at the corners of the graphene rectangles.

The smallest low-energy GP mode is found at the termination of the thin nanoresonator shown in Fig. 2a. It corresponds to the fundamental dipolar edge-plasmon resonance (near-field distribution e1 in Fig. 2a). In the near-field images it manifests as a bowtie-like bright pattern close to the resonator termination. The length of the resonant linear dipole is given by the ribbon width and is only $w = 70$ nm. This results in a deep subwavelength-scale field confinement of better than $\lambda_0/160$ in all three dimensions, yielding an ultra-small mode volume of the order of $10^{-8}\lambda_0^3$.

A particularly interesting near-field distribution (w1 in Fig. 2a) is found when the tip dipole is placed at the centre (D) of the thinnest rectangle (Fig. 2a, middle left). The mode homogeneously extends over the whole resonator width. We explain it by the hybridization of the opposing edge modes e3 (Fig. 2b,c), which spatially overlap when the resonator width becomes smaller than the diameter of the edge modes[24]. In the calculated and experimental near-field images (Fig. 2a, middle right and top right) we recognize this mode by the row of black dots along the centre of the rectangle. Note that the w1 mode corresponds to the fundamental waveguide mode in graphene ribbons with widths $w < \lambda_p/2$, which can be seen, for the first time, in an experimental image (Fig. 2a, top right). This sub-λ_p waveguiding mode could be exploited for the future development of extremely compact subwavelength-scale graphene-plasmonic circuits, such as plasmon interferometers, for sensing and modulator applications.

Besides GP edge modes, we also recognize sheet modes. The transversal fundamental dipolar sheet mode (near-field distribution s1 in Fig. 2a) is recognized in the near-field images of the narrowest rectangle (Fig. 2a). Similar to the near-field images of the smallest disk resonators (Fig. 1b,d), the fundamental dipolar resonance makes the graphene edges appear bright (positive contrast), indicating that the phase shift between the fundamental dipolar GP sheet mode s1 and the tip–substrate near-field interaction is small. With increasing resonator width we observe the evolution to the higher-order sheet modes (near-field distributions s2 and s3), which manifest as bright fringes in the near-field images.

We finally aimed to measure the wavelength and dispersion of the GP edge modes in comparison to sheet modes. For that reason, we study in Fig. 3 a large graphene structure (near-field image shown in Fig. 3a), the size of which exceeds the GP propagation length, thus avoiding Fabry–Perot resonances and sophisticated full spectral analysis[28]. We find that the edge GPs launched by the tip predominately reflect at the corner, manifesting in the near-field image as a black dot located exactly at the corner (Fig. 3a, Fig. 2a–c and Supplementary Section B)[11]. This reflection yields interference patterns in the near-field profiles (dashed curves in Fig. 3b, extracted along the dashed white line in Fig. 3a) similar to those of the sheet plasmons (solid curves in Fig. 3b, extracted along the solid vertical white line in Fig. 3a). Interestingly, the distance Δ_e between the two first minima of the edge profile is shorter than the distance Δ_s observed in the sheet profile, indicating that the wavelength of edge plasmons is shorter than that of sheet plasmons. Although both Δ_e and Δ_s decrease for shorter illumination wavelengths λ_0, their ratio is constant for all λ_0 (symbols in Fig. 3c), in agreement with the quasi-static analytical

approximation for the edge plasmon dispersion in 2D electron gas[23]. For quantifying the wavelength of the edge plasmons, $\lambda_e = \lambda_p \Delta_e/\Delta_s$, we measure the wavelength of the sheet plasmons, λ_p, according to previous works[8,9]. To that end, we measure the distance between the second and third signal maxima of the sheet profiles, yielding $\lambda_p/2$ (as indicated in Fig. 3a,b). The wavelengths obtained for sheet and edge plasmons are summarized in Fig. 3f (red and blue symbols, respectively). A good agreement with theory (solid lines in Fig. 3f, calculated with the help of the mode analysis) is found for a Fermi energy $E_F = 0.33$ eV and a relaxation time $\tau = 0.1$ ps, verifying that with our samples the wavelength scaling of edge plasmons equals that of sheet plasmons. On the other hand, the wavelength of edge plasmons is shorter by a factor of about 1.25, providing a superior field confinement ($\sim\lambda_p/2.5\pi$ in all directions perpendicular to the edge) compared to sheet plasmons ($\sim\lambda_p/2\pi$, only in the vertical direction). We finally corroborate and illustrate our results by calculating the distribution of the near field above the graphene, which is generated when a dipole is placed above the corner (marked by the green dot). The near-field distribution confirms that the wavelength of edge plasmons is shorter than that of sheet plasmons (Fig. 3e). We further find an excellent agreement between the calculated (Fig. 3d, employing the model described above) and experimental (Fig. 3a) near-field images, particularly confirming that the black dot at the corner is due to interference of edge plasmons launched by the tip.

In conclusion, real-space imaging and in-depth analysis of resonant GP modes in nanopatterned graphene structures has revealed a rich variety of plasmon modes that can be categorized as sheet and edge modes. It enabled the observation of ultra-confined resonating edge modes with mode volumes as small as $10^{-8}\lambda_0^3$. We anticipate that real-space analysis of GPs could be of great benefit for the development and quality control of emerging graphene plasmonic technologies, particularly when new design concepts and 2D material heterostructures have to be tested and verified. Further, we believe that the developed understanding of graphene plasmonic near-field contrasts is broadly applicable to other 2D materials. Near-field microscopy could be applied for exploring polariton edge modes in thin films of van der Waals crystals, plasmons in nanopatterned topological insulators, non-reciprocal 1D plasmons[32,33] or plasmons and phonons in mid-infrared and terahertz detectors based on 2D materials and heterostructures, among others.

Methods

Methods and any associated references are available in the online version of the paper.

Received 11 November 2015; accepted 16 February 2016; published online 21 March 2016

References

1. Ju, L. *et al.* Graphene plasmonics for tunable terahertz metamaterials. *Nature Nanotech.* **6,** 630–634 (2011).
2. Yan, H. *et al.* Tunable infrared plasmonic devices using graphene/insulator stacks. *Nature Nanotech.* **7,** 330–334 (2012).
3. Rodrigo, D. *et al.* Mid-infrared plasmonic biosensing with graphene. *Science* **349,** 165–168 (2015).
4. Yan, H. *et al.* Damping pathways of mid-infrared plasmons in graphene nanostructures. *Nature Photon.* **7,** 394–399 (2013).
5. Tamagnone, M., Fallahi, A., Mosig, J. R. & Perruisseau-Carrier, J. Fundamental limits and near-optimal design of graphene modulators and non-reciprocal devices. *Nature Photon.* **8,** 556–563 (2014).
6. Fang, Z. *et al.* Active tunable absorption enhancement with graphene nanodisk arrays. *Nano Lett.* **14,** 299–304 (2014).
7. Fang, Z. *et al.* Gated tunability and hybridization of localized plasmons in nanostructured graphene. *ACS Nano* **7,** 2388–2395 (2013).
8. Chen, J. *et al.* Optical nano-imaging of gate-tunable graphene plasmons. *Nature* **487,** 77–81 (2012).
9. Fei, Z. *et al.* Gate-tuning of graphene plasmons revealed by infrared nano-imaging. *Nature* **487,** 82–85 (2012).
10. Gerber, J. A., Berweger, S., O'Callahan, B. T. & Raschke, M. B. Phase-resolved surface plasmon interferometry of graphene. *Phys. Rev. Lett.* **113,** 055502 (2014).
11. Fei, Z. *et al.* Edge and surface plasmons in graphene nanoribbons. *Nano Lett.* **15,** 8271–8276 (2015).
12. Bermudez-Urena, E. *et al.* Coupling of individual quantum emitters to channel plasmons. *Nature Commun.* **6,** 7883 (2015).
13. Wunsch, B., Stauber, T., Sols, F. & Guinea, F. Dynamical polarization of graphene at finite doping. *New J. Phys.* **8,** 318 (2006).
14. Shung, K. W. K. Dielectric function and plasmon structure of stage-1 intercalated graphite. *Phys. Rev. B* **34,** 979–993 (1986).
15. Hanson, G. W. Dyadic Green's functions and guided surface waves for a surface conductivity model of graphene. *J. Appl. Phys.* **103,** 064302–064308 (2008).
16. Vafek, O. Thermoplasma polariton within scaling theory of single-layer graphene. *Phys. Rev. Lett.* **97,** 266406 (2006).
17. Jablan, M., Buljan, H. & Soljačić, M. Plasmonics in graphene at infrared frequencies. *Phys. Rev. B* **80,** 245435 (2009).
18. Vakil, A. & Engheta, N. Transformation optics using graphene. *Science* **332,** 1291–1294 (2011).
19. Cai, X. *et al.* Plasmon-enhanced terahertz photodetection in graphene. *Nano Lett.* **15,** 4295–4302 (2015).
20. Freitag, M. *et al.* Photocurrent in graphene harnessed by tunable intrinsic plasmons. *Nature Commun.* **4,** 1951 (2013).
21. Koppens, F. H. L. *et al.* Photodetectors based on graphene, other two-dimensional materials and hybrid systems. *Nature Nanotech.* **9,** 780–793 (2014).
22. Zhu, X. *et al.* Plasmon–phonon coupling in large-area graphene dot and antidot arrays fabricated by nanosphere lithography. *Nano Lett.* **14,** 2907–2913 (2014).
23. Volkov, V. A. & Mikhailov, S. A. Edge magnetoplasmons: low frequency weakly damped excitations in inhomogeneous two-dimensional electron systems. *Sov. Phys. JETP* **67,** 1639–1653 (1988).
24. Nikitin, A. Y., Guinea, F., García-Vidal, F. J. & Martín-Moreno, L. Edge and waveguide terahertz surface plasmon modes in graphene microribbons. *Phys. Rev. B* **84,** 161407 (2011).
25. Wang, W., Apell, P. & Kinaret, J. Edge plasmons in graphene nanostructures. *Phys. Rev. B* **84,** 085423 (2011).
26. Yan, H. *et al.* Infrared spectroscopy of tunable Dirac terahertz magneto-plasmons in graphene. *Nano Lett.* **12,** 3766–3771 (2012).
27. Petković, I. *et al.* Carrier drift velocity and edge magnetoplasmons in graphene. *Phys. Rev. Lett.* **110,** 016801 (2013).
28. Schmidt, F.-P. *et al.* Universal dispersion of surface plasmons in flat nanostructures. *Nature Commun.* **5,** 3604 (2014).
29. Ocelic, N., Huber, A. & Hillenbrand, R. Pseudoheterodyne detection for background-free near-field spectroscopy. *Appl. Phys. Lett.* **89,** 101124 (2006).
30. Miroshnichenko, A. E., Flach, S. & Kivshar, Y. S. Fano resonances in nanoscale structures. *Rev. Mod. Phys.* **82,** 2257–2298 (2010).
31. Schuller, J. A. *et al.* Plasmonics for extreme light concentration and manipulation. *Nature Mater.* **9,** 193–204 (2010).
32. Kumar, A. *et al.* Chiral plasmon in gapped Dirac systems. *Phys. Rev. B* **93,** 041413 (2016).
33. Justin, C. W. & Song, M. S. R. Chiral plasmons without magnetic field. Preprint at http://arxiv.org/abs/1506.04743 (2015).

Acknowledgements

The authors acknowledge support from the European Union through ERC starting grants (TERATOMO grant no. 258461, SPINTROS grant no. 257654 and CarbonLight grant no. 307806), the European Commission under the Graphene Flagship (contract no. CNECTICT-604391) and the Spanish Ministry of Economy and Competitiveness (MAT2014-53432-C5-4-R, MAT2012-36580, MAT2012-37638, RYC-2012-12281, FIS2013-47161-P and 'Severo Ochoa' Programme for Centres of Excellence R&D grant no. SEV-2015-0522). F.K. acknowledges support from the Fundacio Cellex Barcelona, the ERC Career integration grant (294056, GRANOP), the EC project GRASP (FP7-ICT-2013-613024-GRASP) and the Government of Catalonia through the SGR grant (2014-SGR-1535).

Author contributions

A.Y.N., P.A.G. and R.H. conceived the study. S.V. patterned the graphene nanoresonators. A.C. and A.P. prepared the CVD graphene. A.Z., F.C. and L.E.H. coordinated the fabrication. P.A.G. and S.M. performed the experiments. A.Y.N. developed the theory and performed the simulations. A.Y.N., P.A.G., F.H.L.K. and R.H. analysed the data and discussed the results. A.Y.N. and R.H. wrote the manuscript with the input of P.A.G. All authors contributed to the scientific discussion and manuscript revisions.

Additional information

Supplementary information is available in the online version of the paper. Reprints and permissions information is available online at www.nature.com/reprints. Correspondence and requests for materials should be addressed to A.Y.N. and R.H.

Competing financial interests

R.H. is a co-founder of Neaspec GmbH, a company producing scattering-type scanning near-field optical microscope systems such as the one used in this study. All other authors declare no competing financial interests.

Methods

Fabrication of graphene resonators. Monolayer graphene samples were grown on a 25-μm-thick copper foil (Cu) catalyst surface within a 4″ chemical vapour deposition (CVD) reactor AIXTRON BM and then transferred onto two different substrates: commercial Si/SiO_2 (300-nm-thick) and CaF_2 onto which a 5-nm-thick-SiO_2 layer was sputtered before graphene transfer. Then graphene resonators of different shapes and sizes were patterned via high-resolution electron beam lithography using a thin PMMA layer, followed by a soft Ar-ion milling for 5 s and resist removal in acetone. See also Supplementary Section C.

Near-field microscopy. Our commercially available s-SNOM (Neaspec, Munich) is based on an atomic force microscope (AFM). The vertically oscillating tip ($\Omega = 250$ kHz, NCSTPt, Nanosensors, Switzerland) acts as a scattering near-field probe. The oscillation amplitude was about 100 nm. P-polarized infrared light from a grating tunable CO_2 laser was focused via a parabolic mirror onto both the tip and sample at an angle of 60° to the surface normal. The tip-scattered light of field E_s was recorded with a pseudo-heterodyne interferometer[29]. To suppress the background scattering from the tip shaft and sample, the detector signal was demodulated at a frequency 3Ω. With this technique we recorded both the amplitude and phase of E_s. All figures show the magnitude of E_s.

Simulation model. The numerical calculations were done using the finite boundary elements method (Comsol). The graphene was modelled as a homogenous 2D conducting layer with the conductivity given by the random-phase approximation[13–17]. The conductivity jumps abruptly to zero at the graphene edge, thus breaking the translation symmetry. We completely neglect contributions from modifications of the electronic spectrum associated with the edge (for example, the electronic edge states and electrostatic effects). This treatment is justified because of the large Fermi energy, yielding large plasmon wavelengths (in the hundred nanometre range) compared with the localization length of electronic edge states (less than one nanometre). The edge plasmons are thus electromagnetic modes based exclusively on collective carrier oscillations. They are confined to the edge, owing to the broken translation symmetry of the conducting 2D sheet. Because of their strong confinement, the edge plasmons exhibit higher momenta than sheet plasmons. Consequently, the dispersions of edge and sheet plasmons are well separated from each other.

The tip was modelled by a vertically (z-) oriented point dipole source to take into account that the experimental tip is an elongated pyramid oriented perpendicular (vertical) to the sample and is illuminated by p-polarized light. Note that the scattering of such a tip can be approximated by an effective dipole of vertical orientation. The scattering of a vertical dipole is proportional to the z component of the electric field below the dipole (note that horizontal fields do not couple to the vertically oriented dipole). We thus simulated the near-field images by calculating the vertical component of the near field below the dipole as a function of the dipole position, scanning the dipole parallel to the substrate above the graphene resonators. This approach is significantly different from previous simulations, where the local density of optical states was calculated[8]. We take into account the phase of the near fields. We are thus able to reproduce both the negative and positive contrast features observed in the experimental near-field images, which have been observed previously but not explained until now.

In the calculations of Fig. 2 we had to vary the Fermi energy in the calculations slightly ($E_F = 0.30$ eV in Fig. 2a, $E_F = 0.28$ eV in Fig. 2b and $E_F = 0.31$ eV in Fig. 2c) to obtain the best agreement with the experimental and calculated near-field images, $|E_s|$ and $|E_z|$, respectively. We explain this need by an inhomogeneous spatial doping of the graphene sheet.

For calculations of the spectra in Fig. 2d–f, the dipole was placed at a fixed position above the resonator, and the near field below the dipole was calculated as a function of λ_0. The spatial near-field distribution of the modes in Fig. 2 were obtained at the following wavelengths λ_0: Fig. 2a: e1 at 11.08 μm, w1 at 11.64 μm, s1 at 10.44 μm; Fig. 2b: e2 at 11.31 μm, e3 at 11.80 μm, s2 at 10.56 μm; Fig. 2c: e4 at 11.32 μm, e3 11.92 μm, s3 at 11.12 μm. They correspond to the peak values found in the spectra of the GP field, obtained by calculating $E_{z,GP} = E_z - E_{z,sub}$. For further details see Supplementary Section A.

We note that the excitation of edge modes by the dipole source can yield plasmon fields inside the resonators, as can be seen for example in the near-field distributions e3 and e4 in Fig. 2c. One explanation for this observation could be the direct coupling of the dipole fields to sheet modes, owing the partial spatial and spectral overlap of edge and sheet modes. Another explanation could be the scattering of edge modes at the corners of the resonators, providing the necessary momentum for coupling edge and sheet modes.